Aerospace Science and Technology 133 (2023) 108145

Contents lists available at ScienceDirect

Aerospace Science and Technology

journal homepage: www.elsevier.com/locate/aescte

Short communication

Enhancing aircraft control surface effectiveness by co-flow jet flap at low energy expenditure

Kewei Xu [a], Gecheng Zha [b,*]

[a] Dept. of Mechanics and Maritime Sciences, Chalmers University of Technology, Gothenburg 41296, Sweden
[b] Dept. of Mechanical and Aerospace Engineering, University of Miami, Florida 33124, USA

ARTICLE INFO

Article history:
Received 11 November 2022
Received in revised form 8 January 2023
Accepted 12 January 2023
Available online 18 January 2023
Communicated by Mehdi Ghoreyshi

Keywords:
Active flow control
Co-flow jet (CFJ)
Separation control
Aircraft control surface
Improved delayed detached Eddy simulation (IDDES)

ABSTRACT

This paper conducts Improved Delayed Detached Eddy Simulation (IDDES) to compare applying co-flow jet (CFJ) active flow control on the flap and on the front main part of an aircraft control surface. Trade studies with varying CFJ momentum coefficients (C_μ) and flap deflection angles (δ) indicate that using CFJ on the flap is much more effective and efficient than applying CFJ on the front main part of the control surface. It is attributed to the feature that CFJ is more advantageous to work in severe adverse pressure gradient (APG). With a small C_μ of 0.025, the configuration with CFJ on the flap achieves a 46.1% increase of lift coefficient (C_L) with an 80.8% lower power consumption compared with the one using CFJ on the front part. Moreover, the control surface with CFJ on the flap can attach the flow very well at a very high deflection angle of 70° and achieves a C_L of 2.5 times larger than that of the baseline control surface.

1. Introduction

Aircraft empennage, including the control surfaces of vertical tails, horizontal tails, and canards, are required to have high control authority with rapid response to keep aircraft trimmed. Control surfaces, thus, have large sizes in general, which brings severe penalties of weight, drag, and energy consumption. In this regard, various active flow control (AFC) methods have been studied to enhance the lift coefficients of control surfaces as the means to reduce their size and weight.

Xu and Zha [1] gave an overview of AFC studies on control surfaces, including the research of Boeing and NASA using synthetic jet [2–4] and sweeping jet actuators [5–9]. An 18% increase of side force (lift) was achieved by the synthetic jet [3], and the sweeping jet was able to increase the side force by 13% to 16% when applied on the Boeing 757 ecoDemonstrator [9].

However, synthetic jets in general lack high momentum to dramatically alter the flows due to their low energy conversion efficiency [10–12], in particular when the main flow has high mass and momentum. The sweeping jets tend to require high power to overcome the high energy loss caused by the jet sweeping and 360° turning of the flow with massive flow separation inside the actuator. Furthermore, the sweeping jet is not a zero-net-mass-flux (ZNMF) flow control and uses engine bleed as the mass flow source. When the engines are idle during landing, they may not be able to provide sufficient mass flow. The same issues also exist for aircraft that do not use jet engines, such as electric aircraft, which are difficult to obtain the air source.

Zhang et al. [13] apply a recently developed ZNMF co-flow jet (CFJ) AFC on a control surface as shown in Fig. 1. The injection slot and suction slot are distributed on both sides of the CFJ control surface airfoil. A micro-compressor actuator is embedded inside to withdraw a small amount of flow from the suction slot, energize it, and inject the flow tangent to the wall near the leading edge. When one side of CFJ is working to generate lift force, the other side of CFJ is closed. Xu and Zha [1] extend the 2D control surface configuration shown in Fig. 1 to a 3D vertical tail, which demonstrates a substantial lift coefficient enhancement at low energy expenditure. The advantage of applying CFJ on the front main part of a control surface as shown in Fig. 1 is that the inner space is larger than the space of the flap. The large space facilitates embedding the CFJ micro-compressor actuators. This is particularly true for small general aviation and unmanned aircraft.

In a control surface, severe adverse pressure gradient (APG) occurs on the deflected flap, and flow separation may occur. The front part of a control surface has smaller or mild APG because it is more aligned with the free-stream flow. Our recent studies on the NASA hump [14,15] indicate that applying CFJ in severe APG is more efficient and effective than in the region of mild APG or fa-

* Corresponding author.
E-mail addresses: kxx50@miami.edu (K. Xu), gzha@miami.edu (G. Zha).

https://doi.org/10.1016/j.ast.2023.108145
1270-9638/

Table 1
Co-flow Jet Parameters.

Parameters	Expressions	Descriptions
Jet momentum coefficient	$C_\mu = \frac{\dot{m}V_j}{\frac{1}{2}\rho_\infty {V_\infty}^2 S}$	$\dot{m}$ is the injection mass flow, V_j is the mass-averaged injection velocity, ρ_∞ and V_∞ denote the free stream density and velocity, and S is the platform area.
CFJ Power consumption	$P = \dot{m}(H_{t1} - H_{t2})$	H_{t1} and H_{t2} are the mass-averaged total enthalpy in the CFJ injection and suction cavities respectively.
CFJ Power in terms of total pressure ratio	$P = \frac{\dot{m}c_p T_{t2}}{\eta}(\Gamma^{\frac{\gamma-1}{\gamma}} - 1)$	Γ is the mass-averaged total pressure ratio between injection and suction cavities, T_{t2} is mass averaged total temperature at suction, c_p is the constant pressure specific heat, γ is the specific heat ratio equal to 1.4 for air, η is the micro-compressor efficiency (For power required, η is taken 100%).
CFJ Power coefficient	$P_c = \frac{P}{\frac{1}{2}\rho_\infty V_\infty^3 S}$	Non-dimensional CFJ power consumption.
Conventional aerodynamic efficiency	$C_L/C_D = \frac{C_L}{C_D}$	C_L and C_D are the lift and drag coefficients.
Corrected aerodynamic efficiency	$(C_L/C_D)_c = \frac{C_L}{C_D + P_c}$	Converting CFJ power coefficient P_c to equivalent drag in order to compare with the conventional configuration.

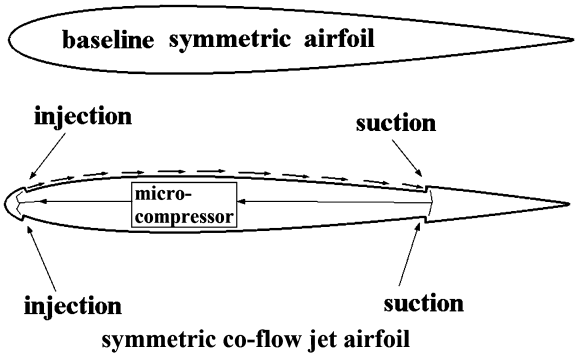

Fig. 1. Schematics of the baseline and the CFJ control surface airfoils.

vorable pressure gradient (FPG). This motivates the present study to apply the CFJ on the flap in severe APG. The purpose is to seek the technique that maximizes the control authority at a lower energy expenditure for aircraft control surfaces. This is the first effort to apply CFJ on an aircraft control surface flap.

2. Co-flow jet parameters

Table 1 lists the important parameters used to evaluate the aerodynamic performance of a CFJ airfoil. The detailed physical meaning of each parameter is explained by Xu and Zha [1] and Lefebvre et al. [16]. The algorithms to calculate lift and drag with jet reactionary forces are described by Zha et al. [17]. The angle of attack of the control surface is varied with the flap deflection angle. Thus, the flap deflection angle effect on the reactionary forces is included in the calculation by the angle of attack.

3. Numerical algorithms

The in-house high-order accuracy CFD code Flow-Acoustics-Structure Interaction Package (FASIP) is used to conduct the numerical simulation. The 3D Improved Delayed Detached Eddy Simulation (IDDES) [1,18–21] turbulence model is used. A 3rd-order WENO scheme for the inviscid flux [22–24] and a 2nd-order central differencing for the viscous terms are employed to discretize the Navier-Stokes equations. The low diffusion Roe scheme used as the approximate Riemann solver is utilized with the WENO scheme to evaluate the inviscid fluxes. Implicit time marching method with dual time stepping using Gauss-Seidel line relaxation is used to achieve a fast convergence rate [25]. Parallel computing is implemented to save wall clock simulation time [26]. The FASIP code is intensively validated for various steady and unsteady flows, including serpentine duct [27], full aircraft [28–30], and CFJ 2D and 3D airfoil simulations [1,16,17,21,28,31–38]. Since the experimental results reported are time-averaged steady-state results, the numerical results are also presented as the time-averaged results after the flow and all the aerodynamic forces become statistically stable.

4. Baseline control surface validation

The baseline control surface model used in the present paper is adopted from the one tested and simulated in [6–9,39]. The baseline vertical tail is tapered, swept with 42° and stacked using NACA0012 airfoil. The aspect ratio based on the mean aerodynamic chord (MAC) is 1.98. The same baseline model is also used in the previous study [1]. The free-stream conditions used are the same as those given by Seele et al. in the experiment [7], which has the Reynolds number Re_∞=1.36×10^6 incoming flow velocity V_∞=40 m/s (about Mach 0.12). The front part of the control surface root is installed on the bottom wall. There is a small clearance between the flap and the wall for the flap deflection, which is simulated in this study as well as in the previous one [1].

The computational domain is meshed using an O-type grid with a mesh size of 6.14 million cells (480 × 80 × 160). The results are stable after a characteristic time of 20 when the standard deviation (SD) of C_L and C_D for the last 200 time-step is in the order of 10^{-9} to 10^{-5}, and are virtually machine zero compared with the C_L and C_D in the order of 1. Details of the mesh topology, boundary condition set-up, and convergence history are given by Xu and Zha [1]. With the present mesh size, the predicted results of the baseline control surface achieve a good agreement with the experimental data with the C_L deviation of 3.8% and C_D deviation of 3.6% considering the massively separated flow due to the 30° deflected flap. More detailed validation of the baseline control surface pressure coefficient distributions (C_p) can be seen in Ref. [1]. Mesh refinement study is conducted by doubling the number of cells in i, j, k direction respectively as 960 × 80 × 160, 480 × 160 × 160 and 480 × 80 × 320. It is demonstrated by Xu and Zha [1] that the numerical results of the baseline control surface are converged based on the mesh size used.

5. 3D CFJ control surface

A 3D CFJ control surface is created based on the baseline configuration by adding an injection slot and a suction slot. The previous study [1] has the CFJ applied on the front main part of the control surface as shown in Fig. 2 (a), which has the injection slot located at 4%C from the leading edge and the suction (blue) slot located at 63%C upstream of the flap. This configuration is named Front CFJ.

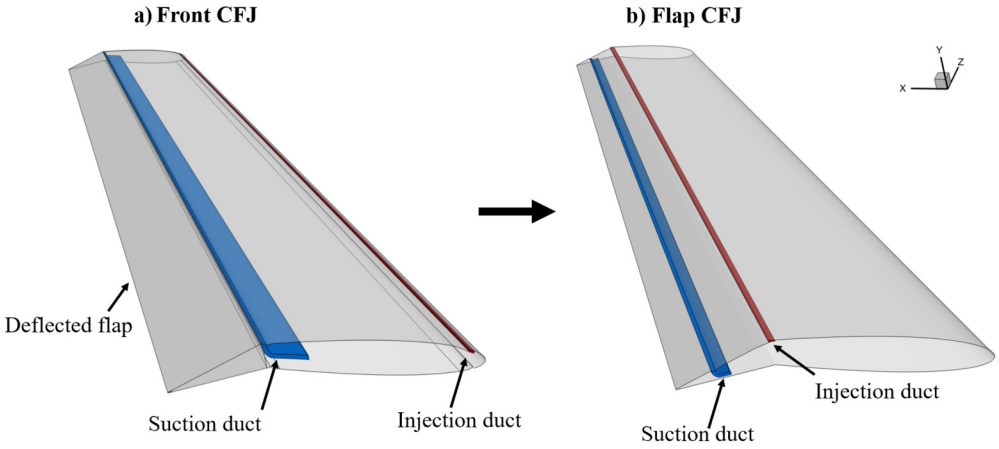

Fig. 2. Geometry of the 3D CFJ control surfaces. (For interpretation of the colors in the figure(s), the reader is referred to the web version of this article.)

Table 2
Mesh refinement studies of the Flap CFJ control surface with C_μ=0.025, β=0°, and δ=30°.

Cases	Mesh size of CFJ	C_L	ΔC_L	C_D	ΔC_D	$(C_L/C_D)_c$	$\Delta(C_L/C_D)_c$
Baseline mesh	125 × 40 × 60	1.096	-	0.114	-	9.243	-
Doubled in i-direction	250 × 40 × 60	1.093	0.28%	0.114	0.40%	9.034	2.20%
Doubled in j-direction	125 × 80 × 60	1.093	0.26%	0.113	1.83%	9.382	1.50%
Doubled in k-direction	125 × 40 × 120	1.101	0.55%	0.115	1.30%	9.227	0.17%

The new configuration studied in this paper is shown in Fig. 2 (b), which has the CFJ applied on the flap with the injection located at 66%C from the leading edge and the suction moved further downstream to 85%C. The new configuration is named Flap CFJ. The injection slot size for the Flap CFJ control surface is 0.45%C, and the suction slot size is 1%C. This study compares these two CFJ implementations in order to identify the better configuration with higher effectiveness and efficiency. The 0.45%C of the Flap CFJ and 0.9%C of the Front CFJ are the results of the optimization to maximize C_L and minimize P_c for the respective configuration. The measure of merits (MoM) used is the corrected aerodynamic efficiency $C_L/(C_D + P_c)$ defined in Table 1. Our trade study indicates that the injection slot size for the Flap CFJ has a very small effect. In this study, we thus keep the injection size fixed at their optimal values

The micro-compressor actuator is not simulated but is numerically treated by applying the compressor boundary conditions (BCs) at the injection duct inlet with total pressure inlet BC and the suction duct outlet with static pressure outlet BC. A specified C_μ is achieved by iterating the injection total pressure. The same mass flow rate of injection and suction is achieved via iterations of the suction outlet static pressure. This CFJ compressor BC has been extensively validated in CFJ serpentine duct [27], CFJ airfoils [16,17,31,32,40], CFJ control surfaces [1], and CFJ micro-compressor with ducts [41,42].

During the cruise, there is no flap deflection. Both the Front and Flap CFJ control surfaces will have no aerodynamic enhancement. However, the open slot steps (the non-continuity of the geometry) will increase drag for both configurations. To avoid the drag created by the open slot steps, our previous study [43] proposes two methods. One method uses small moving plates to cover the open slots. The second method is to let CFJ produce a very light jet to fill the slots. Both methods work very well for the Front CFJ configuration. The same methods are also expected to be applicable to the Flap CFJ cases.

The mesh refinement study is also conducted for the control surface of Flap CFJ. The cases for the mesh refinement study have C_μ=0.025, β=0°, and δ=30°, where β is the side-slip angle and δ is the flap deflection angle. The number of cells in i, j, k directions are doubled respectively for the mesh refinement study. As presented in Table 2, the maximum variations of C_L, C_D and $(C_L/C_D)_c$ (defined in Table 1) are 0.55%, 1.83% and 2.2%, respectively. Fig. 3 compares the C_p distributions at the three spanwise locations where pressure tap rows are embedded in the experiments [39]. The C_p distributions calculated by the initial and refined mesh are virtually overlapped. These results indicate that the CFD simulation achieves mesh-independent solutions.

5.1. Jet momentum coefficient (C_μ) variation

Trade study with the jet momentum coefficients C_μ of 0.025, 0.05, 0.1, 0.2, and 0.26 is conducted to compare the aerodynamic performance of the Front CFJ and Flap CFJ control surfaces. The baseline control surface without CFJ is also presented as a reference. The side-slip angle (β) is fixed at 0°, and the flap deflection angle (δ) is fixed at 30°. Table 3 compares the aerodynamic performance of the baseline, Front CFJ at C_μ=0.025, and Flap CFJ cases at various C_μ. M_j and $\overline{\dot{m}}$ are the injection Mach number and mass flow rate, respectively. Compared with the baseline control surface, both the Front and Flap CFJ cases largely increase the lift coefficient C_L by 28.1% and 46.1% respectively at C_μ of 0.025. Clearly, the Flap CFJ is much more effective in increasing the lift coefficient. Furthermore, the power coefficient of the Flap CFJ is 80.8% smaller than the Front CFJ case. Compared with that of the baseline and Front CFJ configuration, this results in an increase of $(C_L/C_D)_c$ by 32.8% and 30.3%, respectively.

Fig. 4 compares the aerodynamic performance between the Front and Flap CFJ at various C_μ with the data of Front CFJ adopted from our previous work [1]. The baseline case is shown in the blue line as a reference. As shown in Fig. 4 (a), at the small C_μ region below 0.05, the lift coefficient of the Flap CFJ control surface is higher than that of the Front CFJ. This is because applying CFJ at the flap with a high adverse pressure gradient (APG) is more efficient and effective to remove flow separation [14,15]. In fact, at the small C_μ of 0.025 and 0.05, the Flap CFJ achieves a higher improvement of lift (ΔC_L) and corrected aerodynamic efficiency $\Delta(C_L/C_D)_c$ simultaneously compared with the Front CFJ. Fig. 4 (b) shows that both CFJ configurations have C_D reduced with the in-

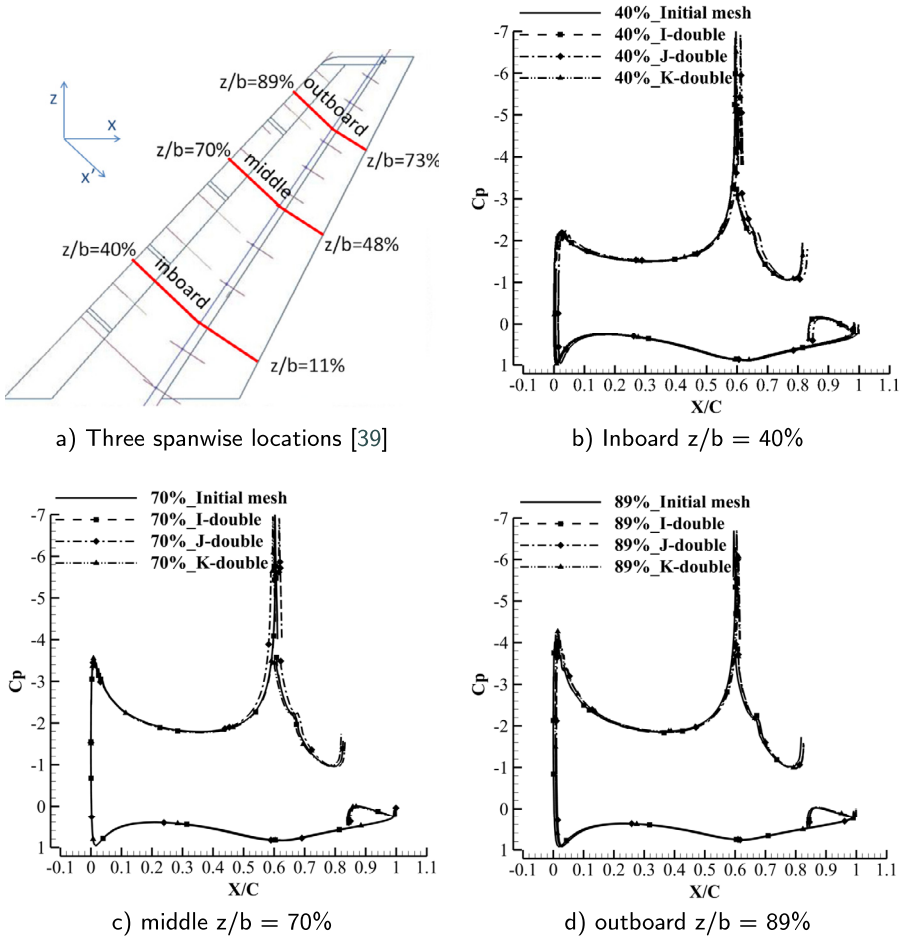

a) Three spanwise locations [39] b) Inboard z/b = 40%

c) middle z/b = 70% d) outboard z/b = 89%

Fig. 3. C_p distributions of the mesh refinement study at inboard, middle, and outboard for the Flap CFJ control surface with C_μ=0.025, β=0°, and δ=30°.

Table 3
Aerodynamic performance of the control surface with different C_μ.

Cases	C_μ	C_L	ΔC_L, %	C_D	P_c	C_L/C_D	$(C_L/C_D)_c$	M_j	$\overline{\dot{m}}$	Γ
Baseline EXP [39]	-	0.78	-	0.112	-	6.96	6.96	-	-	-
Baseline CFD	-	0.75	-	0.108	-	6.93	6.93	-	-	-
Front CFJ	0.025	0.96	28.1	0.109	0.026	8.84	7.09	0.12	0.011	1.02
Flap CFJ	0.025	1.095	46.1	0.113	0.005	9.65	9.24	0.17	0.009	1.006
Flap CFJ	0.05	1.166	55.5	0.115	0.017	10.16	8.85	0.24	0.012	1.013
Flap CFJ	0.1	1.234	64.5	0.104	0.054	11.89	7.79	0.34	0.017	1.030
Flap CFJ	0.2	1.323	76.4	0.076	0.217	17.35	4.51	0.47	0.025	1.083
Flap CFJ	0.26	1.365	82.0	0.056	0.461	24.36	2.64	0.52	0.029	1.154

creasing of C_μ. The power coefficient increases significantly with the increasing C_μ as shown in Fig. 4 (d). This is because P_c is exponentially determined by the total pressure ratio (Γ, Fig. 4 (f)) of the CFJ micro-compressor actuator. Once the flow is attached at C_μ of 0.025, further increasing C_μ without increasing the airfoil camber (i.e., the deflection angle) has a limited benefit on increasing the lift coefficient. But the higher C_μ significantly increases the injection jet velocity (see Table 3), which creates more energy loss for the CFJ system reflected by the increased total pressure ratio Γ.

Since the Flap CFJ achieves both high effectiveness and efficiency at C_μ=0.025, its flow field is compared with the baseline and Front CFJ illustrated by Mach-number-colored streamlines in Fig. 5. Severe flow separation is observed at the flap region of the baseline control surface as shown in Fig. 5 (a). With CFJ applied in the front part as shown in Fig. 5 (b), flow separation at the flap region is largely suppressed, but spanwise flow migration can still be clearly seen. The Flap CFJ has streamlines well aligned in the streamwise direction with very small spanwise flow migration, which also mitigates the tip vortex. This is because applying CFJ near the separation onset location at the flap deflection location is most effective in suppressing flow separation [14,15]. Such high control effectiveness is also evidenced by C_p distributions in Fig. 6. At inboard, middle, and outboard span locations, the Flap CFJ achieves a much lower pressure on the suction surface in the flap region (X/C = 0.63 - 1.0).

5.2. Deflection angle (δ) variation

This section presents the results of the trade study for the flap deflection angle (δ) variation of the Flap CFJ control surface. Results are presented with two C_μ of 0.05 and 0.2 representing the low and high jet intensity, respectively. Four deflection angles of 30°, 40°, 50°, and 70° are studied for the Flap CFJ control surface, the Front CFJ configuration only has the results presented for the deflection angle of 30°, 40°, and 50°, which are adopted from the previous study [1] for comparison.

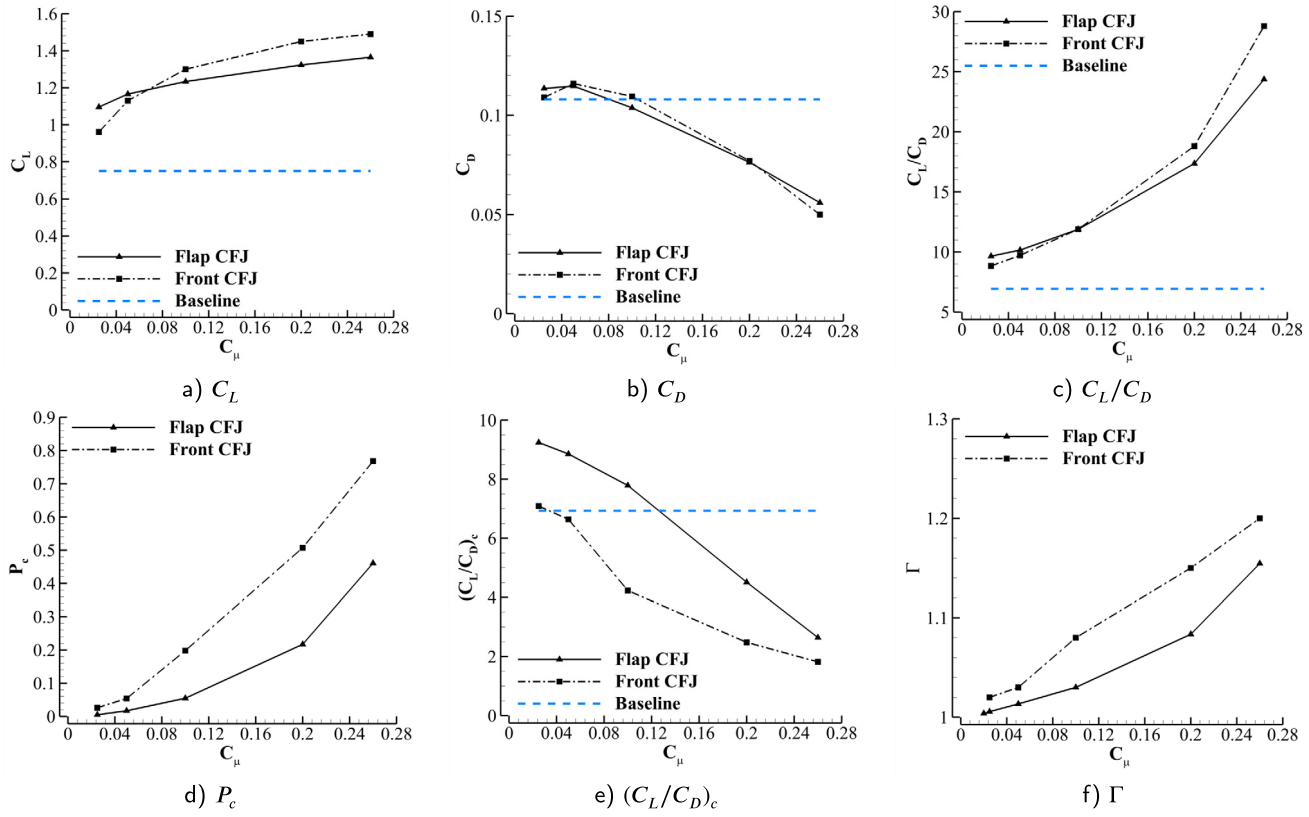

Fig. 4. Comparison of aerodynamic performance between Flap and Front CFJ control surface with various C_μ, β=0°, and δ=30°.

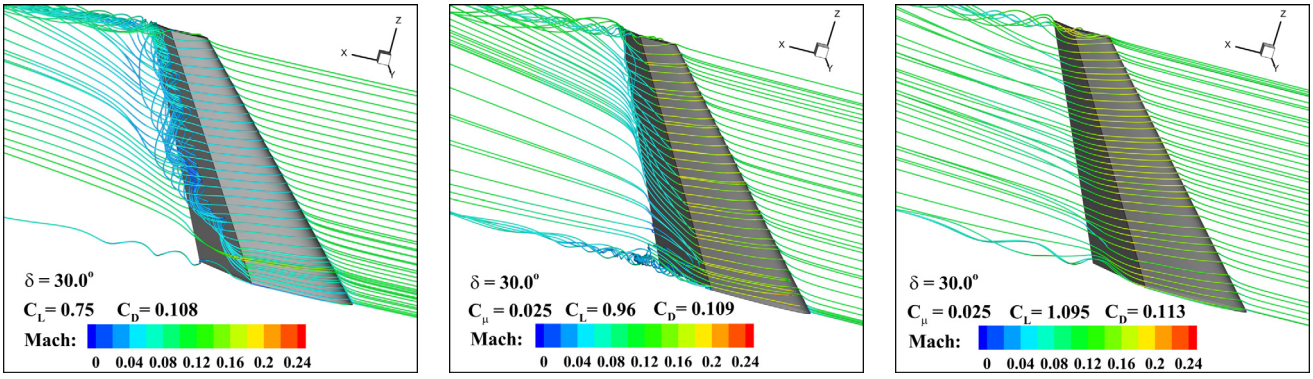

Fig. 5. Streamlines of the baseline and CFJ control surfaces.

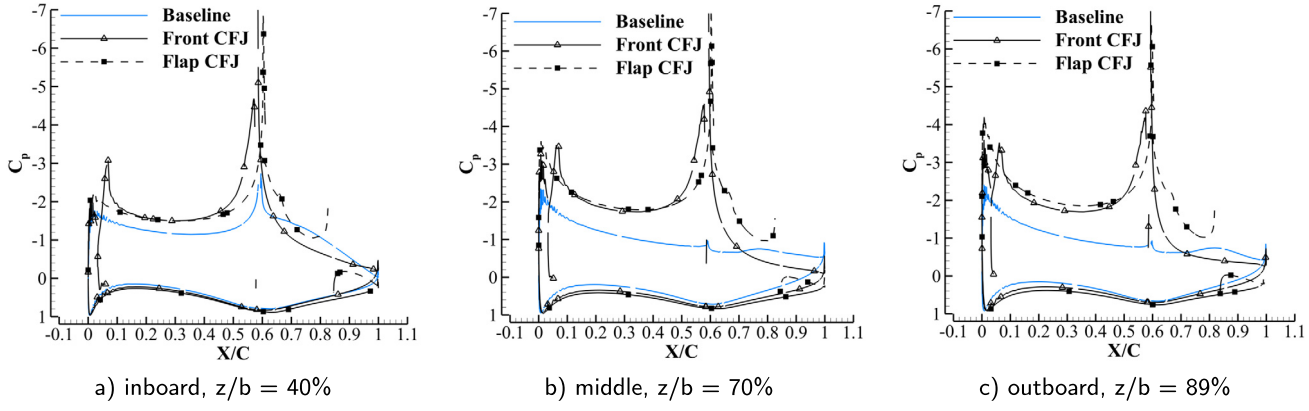

Fig. 6. C_p distribution comparisons of Front and Flap CFJ control surface at inboard, middle, and outboard with C_μ=0.025, β=0°, and δ=30°.

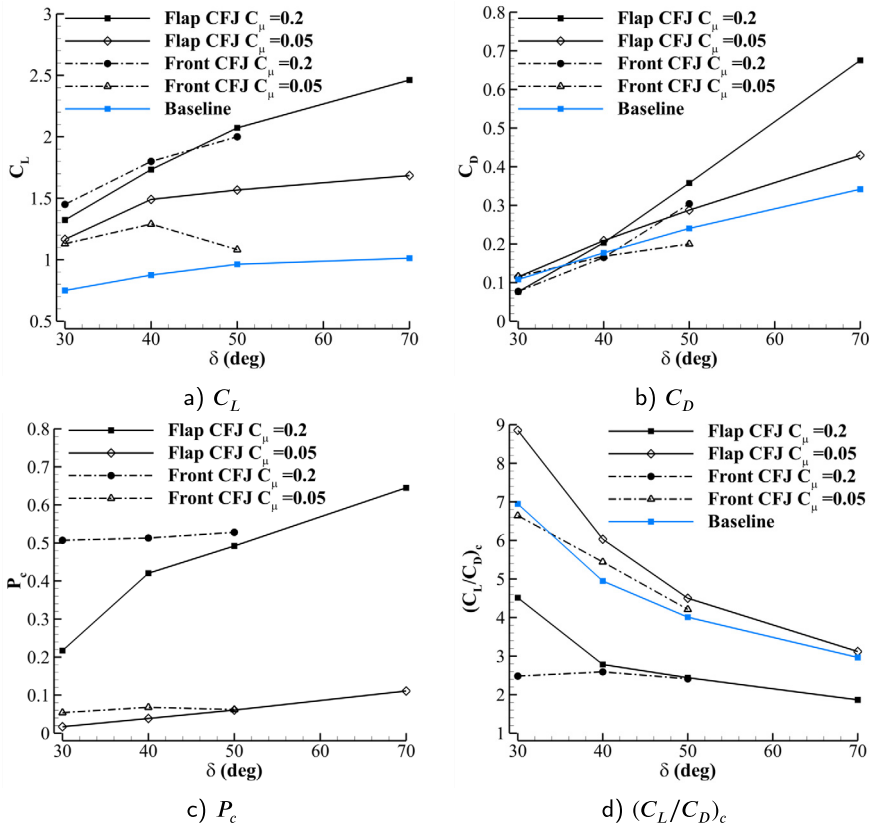

Fig. 7. Comparison of aerodynamic performance between Flap and Front CFJ control surface with various δ, and C_μ of 0.05 and 0.2.

Fig. 7 plots the C_L, C_D, P_c, and $(C_L/C_D)_c$ with the varying δ angles for the Flap CFJ (solid line) and Front CFJ (dashed line) with C_μ of 0.05 (hollow symbols) and 0.2 (solid symbols). The performance of the baseline control surface is plotted by the blue lines. With a small C_μ=0.05 as shown in Fig. 7 (a), Flap CFJ achieves a higher C_L than the Front CFJ in all δ angles due to the effective control of the flow separation at the flap region. The control effectiveness of the Front CFJ at the small C_μ is weakened with an increasing δ because the CFJ applied upstream is not very effective to overcome the high APG downstream. With a high C_μ of 0.2, the Front CFJ has a C_L slightly higher at the δ of 30° and 40°, but is outperformed by the Flap CFJ at a higher δ angle, which is again due to the strong adverse pressure gradient downstream on the flap. For the drag coefficient shown in Fig. 7 (b), both configurations behave similarly with an increasing drag when δ is increased. This is because pressure drag is enlarged as the flap deflects more. With the flap deflection angle increased and the flow remaining attached due to the CFJ, the resultant force, which is mainly from the pressure difference between the suction and pressure surfaces, is also increased and tilted more downstream because of the low pressure on the flap suction surface. Compared with the baseline control surface, the more tilting upstream resultant force of Flap CFJ at a low deflection angle of 30° results in a significantly increased lift and reduced drag as shown in Fig. 7 (a) and (b). At high deflection angles, the large resultant force tilting more downstream generates a substantially higher lift and drag than the baseline case.

The power coefficient (P_c) varying with different δ is shown in Fig. 7 (c). The Flap CFJ has a much lower P_c at low δ angle conditions, about 1/3 of the Front CFJ with C_μ=0.05 and δ=30°. For the same C_μ at δ=40°, the Flap CFJ has the P_c 43.1% lower and the lift coefficient 16.0% higher than the Front CFJ. At δ of 50°, the Front CFJ control surface at C_μ of 0.05 is stalled. The Flap CFJ has a slight flow separation (not shown) with a lift coefficient 44.8% higher than the front CFJ, and the power coefficients are about the same. Such a superior performance of the Flap CFJ results in a substantially higher $(C_L/C_D)_c$ than those of the baseline and the Front CFJ for the whole range of the δ angles from 30°to 70°. Overall, the trade study of the deflection angle indicates that the Flap CFJ is much more effective and efficient to increase the control authority of the control surface at a small C_μ with the power coefficient remaining low.

To further demonstrate the CFJ control effectiveness at high C_μ, Fig. 8 shows the streamlines (colored by Mach number) of the Flap CFJ control surfaces at four deflection angles with C_μ=0.2. The flow in all cases is well attached along the major span except in the tip and root gap vortex regions. Flow accelerates at the locations that the flap deflects, and the acceleration is enhanced with the increasing δ angle due to the attached flows with a higher turning. The observed root vortex is caused by the gap between the deflected flap and the wall, which is intensified as the gap increases at high deflection angles. The tip vortex becomes very strong at δ angle of 70° due to the enhanced pressure difference between the pressure and suction sides of the flap. However, the flow is still very well attached and aligned with the streamwise direction for the majority of the span. The lift coefficient (C_L) at this condition is 2.46, a 125% increase compared with the baseline control surface (baseline C_L=1.09, δ=70°). In principle, a CFJ control surface with 44% size of the baseline control surface can achieve the same lift force, which would bring a substantial weight and drag reduction to the whole aircraft system.

6. Conclusion

A validated numerical study using IDDES is conducted to compare applying CFJ active flow control on the front part of a control

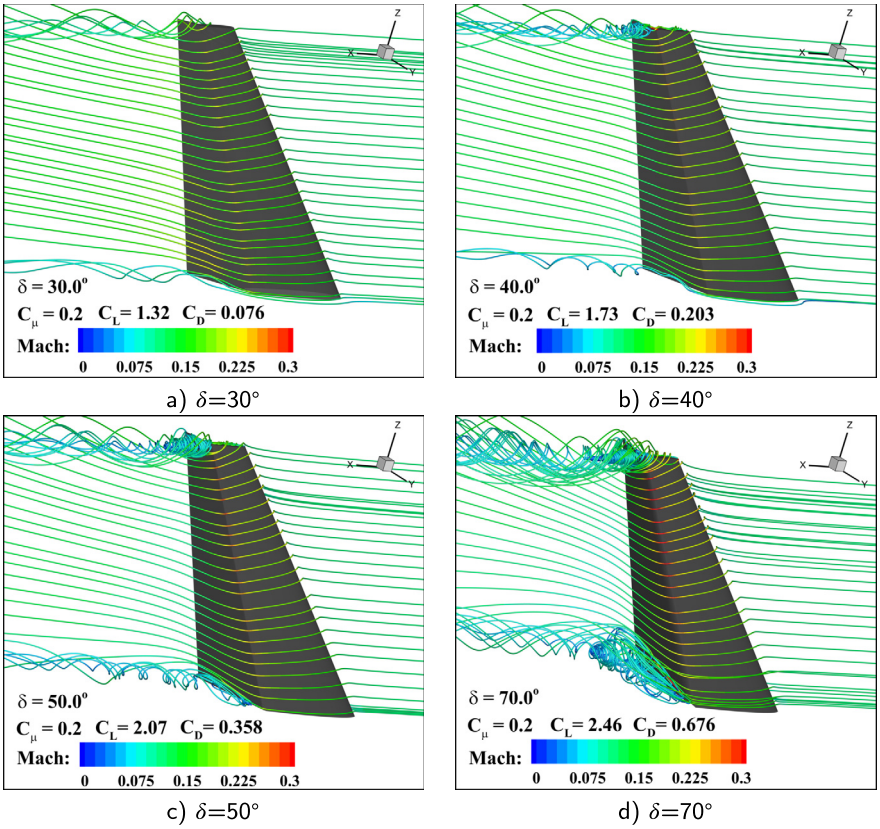

Fig. 8. Streamlines of Flap CFJ cases with various δ and C_μ of 0.2.

surface and on the flap. With a small momentum coefficient (C_μ) of 0.025, the control surface using CFJ on the flap with severe adverse pressure gradient (APG) significantly outperforms the control surface using CFJ in the front main part in both control effectiveness and energy efficiency. The control surface with CFJ flap achieves a 46.1% higher lift coefficient and an 80.8% lower CFJ required power coefficient than those of the Front CFJ configuration. The improvement of the corrected aerodynamic efficiency $\Delta(C_L/C_D)_c$ is increased by 30.3%. The CFJ flap control surface also outperforms the Front CFJ at the high deflection angle (δ) of 50° with C_L increased by 44.8% and $(C_L/C_D)_c$ increased by 6.87%. It can also attach the flow very well at δ of 70° and achieves a lift coefficient about 2.5 times larger than the baseline. Overall, the CFJ flap control surface is much more effective and efficient than the Front CFJ control surface to overcome adverse pressure gradients with attached flow using a small C_μ.

Declaration of competing interest

The authors declare the following financial interests/personal relationships which may be considered as potential competing interests: Gecheng Zha reports a relationship with CoFlow Jet, LLC that includes: equity or stocks.

Data availability

Data will be made available on request.

Acknowledgements

The authors would like to acknowledge the computing resource provided by the Center for Computational Sciences at the University of Miami.

Disclosure: The University of Miami and Dr. Gecheng Zha may receive royalties for the future commercialization of the intellectual property used in this study.

References

[1] K. Xu, G.-C. Zha, High control authority three-dimensional aircraft control surfaces using co-flow jet, AIAA J. Aircr. 2020 (July 2020), https://doi.org/10.2514/1.C035727.
[2] A. Shmilovich, Y. Yadlin, E. Whalen, Computational evaluation of flow control for enhanced control authority of a vertical tail, AIAA J. 45 (8) (2016) 2211–2220, https://doi.org/10.2514/1.J054712.
[3] N.W. Rathay, M.J. Boucher, M. Amitay, E. Whalen, Performance enhancement of a vertical tail using synthetic jet actuators, AIAA J. 52 (4) (2014) 810–820, https://doi.org/10.2514/1.J052645.
[4] N. Rathay, M. Boucher, M. Amitay, E. Whalen, Parametric study of synthetic-jet-based control for performance enhancement of a vertical tail, AIAA J. 52 (11) (2014) 2440–2454, https://doi.org/10.2514/1.J052887.
[5] E. Graff, R. Seele, J.C. Lin, I. Wygnanski, Sweeping jet actuators-a new design tool for high lift generation, in: Innovative Control Effectors for Military Vehicles (AVT-215), Stockholm, Sweden, 20-22 May 2013, 20130013994.
[6] R. Seele, E. Graff, M. Gharib, L. Taubert, J. Lin, I. Wygnanski, Improving rudder effectiveness with sweeping jet actuators, in: AIAA Paper 2012-3244, 6th AIAA Flow Control Conference, New Orleans, Louisiana 25 June 2012 - 28 June 2012, 2012.
[7] R. Seele, E. Graff, J.C. Lin, I. Wygnanski, Performance enhancement of a vertical tail model with sweeping jet actuators, in: AIAA Paper 2013-0411, 51st AIAA Aerospace Sciences Meeting Including the New Horizons Forum and Aerospace Exposition, Grapevine (Dallas/Ft. Worth Region), Texas, 7 January 2013 - 10 January 2013, 2013.
[8] M.Y. Andino, J.C. Lin, A.E. Washburn, E.A. Whalen, E.C. Graff, I. Wygnanski, Flow separation control on a full-scale vertical tail model using sweeping jet actuators, in: AIAA Paper 2015-0785, 53rd AIAA Aerospace Sciences Meeting, Kissimmee, Florida 5-9 January 2015, 2015.
[9] J.C. Lin, M.Y. Andino, M.G. Alexander, E.A. Whalen, M.A. Spoor, J.T. Tran, I. Wygnanski, An overview of active flow control enhanced vertical tail technology development, in: AIAA Paper 2016-0056, 54th AIAA Aerospace Sciences Meeting, San Diego, California, USA 4-8 January 2016, 2016.
[10] W. Crowther, L. Gomes, An evaluation of the mass and power scaling of synthetic jet actuator flow control technology for civil transport aircraft applica-

tions, Proc. Inst. Mech. Eng., Part I, J. Syst. Control Eng. 222 (5) (2008) 357–372, https://doi.org/10.1243/09596518JSCE519.
[11] P. Gil, P. Strzelczyk, Performance and efficiency of loudspeaker driven synthetic jet actuator, Exp. Therm. Fluid Sci. 76 (2016) 163–174, https://doi.org/10.1016/j.expthermflusci.2016.03.020.
[12] Z. Trávníček, J. Kordík, Energetic efficiencies of synthetic jet actuators: commentary on the article by Gil and Strzelczyk, Exp. Therm. Fluid Sci. 98 (2018) 121–123, https://doi.org/10.1016/j.expthermflusci.2018.05.025.
[13] J. Zhang, K. Xu, Y. Yang, Y. Ren, P. Patel, G.-C. Zha, Aircraft control surfaces using co-flow jet active flow control airfoil, in: AIAA Paper 2018-3067, 2018 Applied Aerodynamics Conference, Atlanta, Georgia, June 25-29, 2018, 2018.
[14] K. Xu, Y. Ren, G.-C. Zha, Numerical analysis of energy expenditure for coflow wall jet separation control, AIAA J. 60 (5) (2022) 3267–3285, https://doi.org/10.2514/1.J061015.
[15] K. Xu, Y. Ren, G.-C. Zha, Separation control by co-flow wall jet, in: AIAA 2021 Aviation Forum, AIAA 2021-2946, Virtual Event, June 2021.
[16] A. Lefebvre, B. Dano, W.B. Bartow, M.D. Fronzo, G.-C. Zha, Performance and energy expenditure of coflow jet airfoil with variation of Mach number, J. Aircr. 53 (6) (2016) 1757–1767, https://doi.org/10.2514/1.C033113.
[17] G.-C. Zha, W. Gao, C.D. Paxton, Jet effects on co-flow jet airfoil performance, AIAA J. 45 (2007) 1222–1231, https://doi.org/10.2514/1.23995.
[18] M.L. Shur, P.R. Spalart, M.K. Strelets, A.K. Travin, A hybrid RANS-LES approach with delayed-DES and wall-modelled LES capabilities, Int. J. Heat Fluid Flow 29 (6) (2008) 1638–1649, https://doi.org/10.1016/j.ijheatfluidflow.2008.07.001.
[19] Y. Yang, G.-C. Zha, Simulation of airfoil stall flows using IDDES with high order schemes, in: AIAA Paper 2016-3185, 46th AIAA Fluid Dynamics Conference, Washington, D.C., 13 June 2016, 2016.
[20] Y. Yang, G.-C. Zha, Improved delayed detached Eddy simulation of super-lift coefficient of subsonic co-flow jet flow control airfoil, in: AIAA Paper 2018-0314, 2018 AIAA Aerospace Sciences Meeting, Kissimmee, Florida, 8-12 January 2018, 2018.
[21] B. Wang, G.-C. Zha, Detached-Eddy simulation of a coflow jet airfoil at high angle of attack, J. Aircr. 48 (5) (2011) 1495–1502, https://doi.org/10.2514/1.C000282.
[22] Y.-Q. Shen, G.-C. Zha, B. Wang, Improvement of stability and accuracy of implicit WENO scheme, AIAA J. 47 (2009) 331–334, https://doi.org/10.2514/1.37697.
[23] Y.-Q. Shen, G.-C. Zha, X.-Y. Chen, High order conservative differencing for viscous terms and the application to vortex-induced vibration flows, J. Comput. Phys. 228 (2) (2009) 8283–8300, https://doi.org/10.1016/j.jcp.2009.08.004.
[24] Y.-Q. Shen, G.-C. Zha, Improvement of the WENO scheme smoothness estimator, Int. J. Numer. Methods Fluids (2009), https://doi.org/10.1002/fld.2186.
[25] G.-C. Zha, E. Bilgen, Numerical study of three-dimensional flows using unfactored upwind-relaxation sweeping algorithm, J. Comput. Phys. 125 (2) (1996) 425–433, https://doi.org/10.1006/jcph.1996.0104.
[26] B. Wang, Z. Hu, G.-C. Zha, General subdomain boundary mapping procedure for structured grid implicit CFD parallel computation, J. Aerosp. Comput. Inf. Commun. 5 (11) (2008) 425–447, https://doi.org/10.2514/1.35498.
[27] K. Xu, G.-C. Zha, System energy benefit using co-flow jet active separation control for a serpentine duct, Aerosp. Sci. Technol. 128 (2022) 107746.
[28] A. Lefebvre, G.-C. Zha, Design of high wing loading compact electric airplane utilizing co-flow jet flow control, in: AIAA Paper 2015-0772, AIAA SciTech2015: 53rd Aerospace Sciences Meeting, Kissimmee, FL, 5-9 Jan 2015, 2015.
[29] J. Gan, Y.-Q. Shen, G.-C. Zha, Comparison of drag prediction using rans models and ddes for the dlr-f6 configuration using high order schemes, in: 54th AIAA Aerospace Sciences Meeting, AIAA 2016-0553, 2016, p. 0553.
[30] Y. Yang, G.-C. Zha, Numerical investigation of performance improvement of the co-flow jet electric airplane, in: AIAA Paper-2018-4208, AIAA AVIATION Forum, AIAA 2018-4208, vol. 2018, 2018, pp. 25–29.
[31] G.-C. Zha, C. Paxton, A. Conley, A. Wells, B. Carroll, Effect of injection slot size on high performance co-flow jet airfoil, AIAA J. Aircr. 43 (2006) 987–995, https://doi.org/10.2514/1.16999.
[32] B. Wang, B. Haddoukessouni, J. Levy, G.-C. Zha, Numerical investigations of injection-slot-size effect on the performance of coflow jet airfoils, J. Aircr. 45 (6) (2008) 2084–2091, https://doi.org/10.2514/1.37441.
[33] Z.-X. Liu, G.-C. Zha, Transonic airfoil performance enhancement using co-flow jet active flow control, in: AIAA Paper 2016-3066, AIAA Aviation, Washington, D.C., June 13-17 2016, 2016.
[34] A. Lefebvre, G.-C. Zha, Trade study of 3D co-flow jet wing for cruise and take-off/landing performance, in: AIAA Paper 2016-0570, AIAA SCITECH2016, AIAA Aerospace Science Meeting, San Diego, CA, 4-8 January 2016, 2016.
[35] Y. Yang, G.C. Zha, Super-lift coefficient of active flow control airfoil: what is the limit?, in: AIAA Paper 2017-1693, AIAA SCITECH2017, 55th AIAA Aerospace Science Meeting, Grapevine, January 9-13 2017, 2017.
[36] H.-S. Im, G.-C. Zha, B.P.E. Dano, Large Eddy simulation of coflow jet airfoil at high angle of attack, J. Fluids Eng. 136 (2) (2014) 021101, https://doi.org/10.1115/1.4025649.
[37] H.-S. Im, G.-C. Zha, Delayed detached Eddy simulation of airfoil stall flows using high-order schemes, J. Fluids Eng. 136 (11) (2014), https://doi.org/10.1115/1.4027813.
[38] Z. Lei, G.-C. Zha, Lift enhancement for supersonic delta wing at low speed using coflow jet, in: AIAA Aviation and Aeronautics Forum and Exposition, AIAA AVIATION Forum 2021, American Institute of Aeronautics and Astronautics Inc, AIAA, 2021, pp. AIAA–2021.
[39] V.N. Vatsa, D. Casalino, J.C. Lin, J. Appelbaum, Numerical simulation of a high-lift configuration with embedded fluidic actuators, in: AIAA Paper 2014-2142, 32nd AIAA Applied Aerodynamics Conference, Atlanta, GA, 16-20 June 2014, 2014.
[40] G. Zha, Y. Yang, Y. Ren, B. McBreen, Super-lift and thrusting airfoil of coflow jet actuated by micro-compressors, in: 2018 Flow Control Conference, Atlanta, Georgia, June 25-29, AIAA 2018-3061, 2018.
[41] P.A. Barrios, Y. Ren, K. Xu, G.-C. Zha, Design of 3d co-flow jet airfoil with integrated micro-compressor for high operating efficiency at cruise condition, in: AIAA Aviation 2021, Washington, D.C., AIAA 2021-2581, 7-11 June 2021, 2021.
[42] K. Xu, G.-C. Zha, Design of high specific speed mixed flow micro-compressor for co-flow jet actuators, GT2019-90980, in: GT2019-90980, IGTI Turbo Expo 2019, Phoenix, Arizona, USA, June 17 - 21, 2019, 2019.
[43] K. Xu, J. Zhang, G. Zha, Drag minimization of co-flow jet control surfaces at cruise conditions, in: AIAA 2019-1848, AIAA Scitech 2019 Forum, San Diego, California, 7-11 January 2019, 2019.